Structure and strength of sub-100 nm lamellar structures in cold-drawn pearlitic steel wire

Zhang, Xiaodan; Hansen, Niels; Godfrey, Andrew ; Huang, Xiaoxu

Published in:
Materials Science and Technology

Link to article, DOI:
10.1080/02670836.2018.1440155

Publication date:
2018

Document Version
Peer reviewed version

Structure and strength of sub-100 nm lamellar structures in cold-drawn pearlitic steel wire

Xiaodan Zhang [1, 2], Niels Hansen [2], Andrew Godfrey [3] and Xiaoxu Huang [2, 4]

[1] *Section for Manufacturing Engineering, Department of Mechanical Engineering, Technical University of Denmark, 2800 Kgs. Lyngby, Denmark*
[2] *Section for Materials Science and Characterization (MAC), Department of Wind Energy, Technical University of Denmark, DK-4000, Roskilde, Denmark*
[3] *Key Laboratory of Advanced Materials (MOE), School of Materials Science and Engineering, Tsinghua University, Beijing, 100084, PR China*
[4] *Section for Materials and Surface Engineering, Department of Mechanical Engineering, Technical University of Denmark, 2800 Kgs. Lyngby, Denmark*

Corresponding author: Xiaodan Zhang, Senior Researcher, Section for Manufacturing Engineering, Department of Mechanical Engineering, Technical University of Denmark, 2800 Kgs. Lyngby, Denmark. xzha@mek.dtu.dk

Please cite this paper as following: Xiaodan Zhang, Niels Hansen, Andrew Godfrey & Xiaoxu Huang (2018): Structure and strength of sub-100 nm lamellar structures in cold-drawn pearlitic steel wire, Materials Science and Technology
To link to this article: https://doi.org/10.1080/02670836.2018.1440155

Structure and strength of sub-100 nm lamellar structures in cold-drawn pearlitic steel wire

Pearlitic steel wire, with a representative sub-100 nm lamellar structure, is the strongest mass-produced steel with an excellent combination of formability and strength. This overview summarizes investigations of cold-drawn pearlitic steel wire in the last decades, covering the microstructural evolution and strengthening mechanisms. Based on quantitative structural parameters, this overview covers a quantitative and extensive analysis of structure-strength relationships. By focusing on the structure, challenges and future strategy are outlined to further improve the mechanical behavior and performance of pearlitic steel wire to widen its use in society.

Keywords: Pearlitic steel wire; sub-100 nm lamellar structure; Strengthening mechanisms; Strength-structure relationship; Dislocation-based plasticity;

1. Introduction

In the history of mankind, the development of strong materials has been pursued through ages with names illustrating the progress [1]. Processing has been followed by analysis of strengthening mechanisms, and it has been found almost as a rule of nature that a structural refinement leads to an increase in strength.

It has also been found that this rule may apply towards the limit which is a structure on the nanoscale and a strength approaching the theoretical limit which is $E/10$, where E is the elastic modulus. Examples are martensitic and bainitic steel produced by phase transformation but ultrastrong steel can also be produced by plastic deformation [2-4] where deformed pearlitic steel is presented in this overview focusing on the structure and strength of steel with sub-100 nm lamellar structure in cold-drawn pearlitic steel wire containing 0.8 wt.% C (3.6 at. % C).

The history of such wires dates back to 1886 [5] when wires with a carbon content of 0.828 wt.% and a strength not less than 1.65 GPa were produced for military applications. Since then, super strong wire with good formability, high strength with acceptable ductility, continuous work hardening with high rate and no yield point (figure 1), have found wide applications as musical strings, bridge suspension cables, steel cords for automobile tires, springs and most recently as saw wires for photovoltaic solar cells. Today the strongest commercial wires reach a strength of 4.5 GPa [6] compared to 6.8 GPa [7] for experimental samples.

The technological and scientific progress has over the years been reported in many research papers [6-11] supplemented by review papers where the latest one is from 2016 [12]. In the present paper the field will be narrowed to cover an analysis of the microstructural morphology and a quantification of microstructural parameters in

Please cite this paper as following: Xiaodan Zhang, Niels Hansen, Andrew Godfrey & Xiaoxu Huang (2018): Structure and strength of sub-100 nm lamellar structures in cold-drawn pearlitic steel wire, Materials Science and Technology
To link to this article: https://doi.org/10.1080/02670836.2018.1440155

sub-100 nm structures. The structural overview is followed by an introduction and discussion of strengthening mechanisms where three have been identified: boundary strengthening, dislocation strengthening and solid solution hardening [9]. In a following section the flow stress of wires is derived based on an assumption of additive contributions from the three strengthening mechanisms. This assumption is validated by comparison with experimental measurement of the flow stress. In a final section the model will be discussed leading to an outlook covering materials, process design and advancement of characterization techniques both in 2D, 3D and 4D. Thereby a firm basis will be created for analytical and numerical (mathematical) analysis covering processing, structure and properties including performance of superstrong wires in different environments.

2. Structural evolution in the strain range 0-5.4

Lamellar pearlite with alternating layered ferrite and cementite is formed by the isothermal decomposition of eutectoid austenite. Several differently oriented pearlite colonies are formed within one former austenite grain during a process called patenting [13]. The microstructural parameters (see figure 2) including interlamellar spacing (ILS), the thickness of cementite (T) and the thickness of ferrite (F), show dependence on the patenting temperature for isothermal growth conditions and on the translation velocity for forced-velocity growth conditions [11, 13]. Here the pearlite colony is defined as an area with a similar ferrite crystallographic orientation and continuous/discontinuous cementite lamellae which are easy to differentiate in the SEM/TEM at low and medium strains ($0 < \varepsilon \leq 1.5$) in a 0.8 wt.% pearlitic steel wire [14, 15], as shown in figure 2a. Previous work has shown that significant structural changes take place during the wire drawing of the patented intermediate rods with a diameter of several millimeters to a final diameter of several tens of micrometers. These structural changes are primarily the reorientation of the initial random lamellar structure to the drawing direction [9, 11, 14-29], and at large strains a well-developed lamellar nanoscale structure which characterizes the longitudinal section and a typical curled structure associated with drawing of a BCC metals which characterizes the cross section [18, 22, 30-32], as shown in figure 2b and 2c. The structural evolution from low to high strain involves processes as reorientation, deformation and decomposition of cementite, and reorientation and deformation of the ferrite phase. In parallel, the ferrite is plastically deformed and dislocations are stored in different configurations from threading dislocations to dislocation cell boundaries.

The structural evolution is hierarchical as the strain is increased but the rate of evolution shows a transition between two regions below and above the strain range 2.7 – 3.4. The transition is related to breakage and decomposition of cementite increasing significantly the carbon concentration in the ferrite, as illustrated by cementite thickness evolution (see section 3.1). A further increase in strain beyond 3.7 leads to a significant structural change as illustrated in figure 3. The ferrite microstructure refines, and the cementite lamellae deform to the limit and start to break-up from a lamellar morphology to a plate morphology with platelets distributed along the interface between neighboring ferrite lamella at a strain of 5.4 (figure 3b), with the limit of cementite thickness around 0.6 nm (see figure 12) which is close to the critical edge length of an original cementite unit cell [11].

Please cite this paper as following: Xiaodan Zhang, Niels Hansen, Andrew Godfrey & Xiaoxu Huang (2018): Structure and strength of sub-100 nm lamellar structures in cold-drawn pearlitic steel wire, Materials Science and Technology
To link to this article: https://doi.org/10.1080/02670836.2018.1440155

2.1 Reorientation of cementite in the drawing direction

The evolution of the size and shape of the pearlite colony during cold drawing has been investigated [29] by adopting an ellipsoidal geometric model, and the results demonstrate that the progressive cold drawing slenderizes the pearlitie colony with a clear enlargement of the main axis quasi-parallel to the drawing direction and a shortening of the axis perpendicular to the former. The cementite plates have been used as markers and the statistics on the macroscopic orientation and length in the longitudinal section and on the length of cementite plates/particles in the transverse sections has been obtained [19]. Pearlite colonies are classified into type I (0° – 30°), II (30° – 60°), and III (60° – 90°), three macroscopic orientation classes, according to the angle between the cementite lamellar direction in the longitudinal section and the wire axis, and five length classes. Between $\varepsilon = 0$ and $\varepsilon = 1.5$ the percentage sum of the cementite lamellae in each length range in the longitudinal section remains almost the same, whilst the alignment changes. As a result of this process, more than half of the cementite lamellae have rotated towards the drawing axis in the longitudinal section at $\varepsilon = 1.5$. At higher strain the cementite lamellae become aligned parallel to the drawing direction with an angular spread of 30° (97% at a strain of 1.5, 100% at a strain of 3.7) and are lengthened as seen in the longitudinal plane (figure 4). These experimental results have been compared with the calculations based on (i) uni-axial stretching and (ii) plane strain stretching models [18]. By comparing the percentage data of three types of structures at different strains, the plane strain assumption seems to be closer to the reality than the simple tension assumption for Type I structure. Even so, the differences between the experimental data and the calculated values under both assumptions show that supplementary mechanisms may operate.

The deformation of pearlite lamellar structure is strongly connected with plastic deformation of the ferrite including curling which is typically observed in the cross section of bcc metallic wires [17, 18, 21, 29, 30, 32], which shows that dislocation slip takes place in the ferrite and then transmits into the cementite. Based on these observations in the longitudinal section, five evolution paths to change thickness and macroscopic orientation of the ferrite lamellae, have been proposed [15] in figure 5. A, type I structure in the original patented wire (see Table 1), shows a favourable lamellar orientation to the wire axis since the plates will not act as strong barriers for dislocation slip in the ferrite lamellae which will deform uniformly with a good approximation. In contrast when the lamellae are inclined or perpendicular to the wire axis in B and C (type II and III structures in the original patented wire), the applied deformation will cause twisting, kinking, and breakup of cementite platelets, resulting in a rigid body rotation. At high strains the lamellar structure becomes aligned to the drawing direction and the ferrite lamellae are thinned and lengthened with increasing strain. These evolution paths of the initial structures with different macro-orientation to the drawing direction in the initial patented wire, illustrate a hierarchical evolution of the deformation structure with increasing strain, which can lead to through-diameter reorientation in morphology and crystallography.

2.2 Through diameter reorientation

The through diameter reorientation during wire drawing has been investigated by the combination of SEM and EBSD and the definition of the different structures is shown in

Please cite this paper as following: Xiaodan Zhang, Niels Hansen, Andrew Godfrey & Xiaoxu Huang (2018): Structure and strength of sub-100 nm lamellar structures in cold-drawn pearlitic steel wire, Materials Science and Technology
To link to this article: https://doi.org/10.1080/02670836.2018.1440155

Table 1. Based on visual inspection of pairs of SEM and EBSD images from the same locations in the longitudinal section, three different structural types from type A, B and C structures in the original patented wire may be identifiable in the drawn wire at low and medium strains: a) A_A represents the deformation structure coming from A pearlite colonies in the patented wire; b) A_B and A_C represent the deformation structure originating from colonies B and C in the patented wire; c) A_B and A_C structures can be easily identified based on their high content of kinking, shear bands, S-bands, and high density of high angle boundaries in the ferrite at low to medium strains, in comparison with A_A structures which keep the lamellar structure parallel to the drawing direction except for few shear bands. However at a strain around 1.5, A_B and A_C structures are no longer clearly distinguished and they are sorted together into A_BC structures.

At strains larger than 1.5, morphological differences cannot used as a criterion to separate A_A and A_BC structures due to a uniform morphology. However, by measuring ferritic misorientation angles along and across the lamellae, it has been found that the uniform structure has been subdivided into volume elements with very different crystallographic characteristics. An example is shown in figure 6 that part of the volume is divided by lamellar boundaries with high misorientation angles across which can reach 40^{o} in figure 6c. However, other areas in this volume only show low angle boundaries less than 15^{o}. This significant difference suggests a structural subdivision into A_A and A_BC structures where A_A structures are undergoing almost uniform deformation, and only subdivide by the formation of low angle boundaries. A misorientation angle profile measured along the ferrite lamellae is shown in figure 6d for A_A structures and in figure 6e for A_BC structures. The misorientation angles are small however significantly larger in A_BC structures than in A_A structures.

In figure 7 the observations in figure 6 are confirmed in the form of pole figures which illustrate spread crystal rotations around the wire axis (figure 7b and 7c) characterizing the A_BC structure where only small rotations are present in the A_A structures (figure 7d and 7e). This crystal rotation around the wire axis suggests that A_BC structures may relate to the curling (see figure 2) which may take place as part of the reorientation of B and C structures.

The EBSD characterization has been followed by a quantification of the average interlamellar spacing (ILS) for the initial A, B and C structures and for A_A and A_BC structures in the strain range from 1.5 to 3.7, as shown in Figure 8. This figure also includes the calculated ILS based on the assumption that ILS is reduced in accordance with the wire diameter [8, 9, 11, 19]. The calculated value is in good agreement with the experimental ones for the A_A structure but underpredicts the ILS for the A_BC structure.

2.3 Deformation and decomposition of cementite

Cementite, has an orthorhombic structure [33]. The bulk cementite has a known inherent brittleness due to an insufficient number of slip systems. However, the ability of constrained cementite to sustain plastic deformation has been widely demonstrated in the pearlitic steel via replica observations of slipped lamellae [34], indirect evidence of cementite plate thinning [9, 11, 16, 20-24], cementite subdivision/fragmentation [16, 20,

Please cite this paper as following: Xiaodan Zhang, Niels Hansen, Andrew Godfrey & Xiaoxu Huang (2018): Structure and strength of sub-100 nm lamellar structures in cold-drawn pearlitic steel wire, Materials Science and Technology
To link to this article: https://doi.org/10.1080/02670836.2018.1440155

35, 36] and direct observation of dislocation structures and plane defects by transmission electron microscopy [37-47].

As the microstructure gets finer with the decrease of patenting temperature, the interlamellar spacing decreases down to less than 100 nm and the thickness of cementite is below 20 nm. This microstructure refinement will increase the deformation compatibility between ferrite and cementite which is demonstrated by relatively homogeneous slip in both cementite and ferrite during the tensile deformation of the fine pearlites [48] and simultaneous thickness decrease of ferrite and cementite lamellae during drawing [9, 11, 16, 20, 21, 23, 24]. This deformation compatibility up to the drawing strain of 2.7, has been demonstrated in the obervations where coarse slip steps, S-bands and cracks across cementite parallel to {110}a-Fe or {112}a-Fe plane traces in drawn pearlitic wires [21, 22] as shown in figure 9 and slip on $(12\bar{1})Fe_3C//(\bar{1}10)$ α-Fe in 10% cold rolled pearlitic steel sheets [49]. This deformation compatibility has also been shown by the work-hardening with the increase of dislocation density (Table 3) and by subdivision of nano-sized cementite where cementite lamellae become composed of smaller crystals as shown in figure 10. The further subdivision of the nano-sized cementite lamellae/plates into (sub-)nano cementite crystals can easily produce diffraction rings in the selected area diffraction pattern, which is stated in literature "the cementite turns amorphous" [50-52]. The increased deformability of nano-sized cementite may indicate more activated slip systems and/or stacking faults with other defects. However, this breakage, refinement and subdivision of the cementite as well as the structural and chemical change, also compounds the difficulty in the characterization where the sample preparation for HREM is very critical. The typical sample thickness around several tens nanometers may not work for the HREM characterization of (sub-) nanometer cementite crystals. The deformation mechanisms of the nano-size cementite may be investigated by advanced characterization combining TEM, atomic-scale HREM and 3DAPT, complemented by molecular dynamics simulations and first-principles calculations based on density functional theory (DFT) [53].

Decomposition of cementite during the plastic deformation of steels where the stoichiometric carbon content is less than 25 at.%, has been detected by various techniques, such as mössbauer spectrometry [54-56], thermomagnetic analysis [55, 57], internal friction [55], electron energy loss spectrometry [58] and atom probe microscopy [7, 10, 51, 59-62]. Basically, two causes for the destabilization and decomposition of cementite have been proposed: (i) a higher binding enthalpy between carbon atoms and dislocations in ferrite as compared with the binding of carbon and iron atoms in cementite [54]; (ii) an increase of its free energy arising from thinning and breakage of cementite lamellae and creation of slip steps during wire drawing [58]. Based on observations where nanoscale and coarse slip steps, S-bands and cracks across cementite parallel to {110}a-Fe or {112}a-Fe plane traces in drawn pearlitic wires [21, 22] as shown in figure 9, a third mechanism can be that the dislocations slip pass or cut through the cementite lamellae and drag the carbon atoms to the ferrite/cementite interfaces or into the ferrite lamellae. However, which one is dominating is still in debate where it may also be taken into account that the deformation of nanoscale cementite and either high angle or low angle boundaries left behind by a complete decomposition of cementite confirmed by the crystallographic orientation measurements across the ferrite lamellae as discussed in Section 2.2. When the drawing

Please cite this paper as following: Xiaodan Zhang, Niels Hansen, Andrew Godfrey & Xiaoxu Huang (2018): Structure and strength of sub-100 nm lamellar structures in cold-drawn pearlitic steel wire, Materials Science and Technology
To link to this article: https://doi.org/10.1080/02670836.2018.1440155

strain is beyond 3, the 3DAP measured carbon content of the cementite lamellae (with the thickness between 3 nm to 8 nm) ranges from 12 at.% to 22 at.% [10]. When the strain is higher, the thickness of cementite lamellae decreases as well as the carbon concentration, as shown in figure 11 [61]. However, even at the strain up to 5.4, the authors still observed the cementite lattices with the particle/plate shape, which indicates the stability of the cementite structure in accordance with the statement "cementite should be regarded as an phase Fe_3C_{1-x} with x = 0- 0.5" [63, 64].

2.4 Texture

It is well documented that during wire drawing of pearlitic steels a <110> fiber texture develops and gets stronger with the drawing strain up to the strain around 3 [16, 19, 25, 65-73]. Except for this <110> fiber texture, the detailed information on the texture components in the wire at a higher strain is very limited due to the fineness of the microstructure and limitations of the applied techniques: i) the traditional EBSD does not work due to a much larger activation volume diameter than 20 nm, the value of ILS at the strain around 3; ii) the transmission EBSD requires a "clean" crystal in the beam direction where the sub-grain or dislocation boundaries are not welcome, which makes the sample-making extremely difficult; iii) the neutron/symchrotron/X-ray diffraction methods only give the average value of activated volume (with a diameter from several hundreds of nanometers to several tens of micrometers) which limits the analysis of micro-texture components; iv) the nanobeam TEM diffraction method needs very careful data collecting and analysis which is time-consuming.

3. Structural parameters

The two phases in the pearlitic steel, ferrite and cementite undergo significant changes in structural morphology and structural parameters with increasing strain. To analyze and quantify the strengthening mechanisms, a systematic detailed microstructural characterization is vital to provide the evaluation base. The key microstructural parameters in the deformed pearlitic steel are the ILS, the thickness of ferrite lamellae (F), the thickness of cementite lamellae (T), the dislocation density in the ferrite lamellae and the carbon enrichment in the ferrite lamellae due to cementite decomposition at large strains.

3.1 Evolution of ILS, F and T

The evolution rule of ILS with the drawing strain shown as equation (1), was first proposed by Embury and Fisher [8] that the mean barrier spacing is reduced in proportion to the wire diameter on the assumption that no new barriers are generated or existing barriers destroyed, while the deviation with the mean measured value is shown in the wires with strains < ~ 1.5. This deviation at low and medium strains has also been observed in the wires with the drawing strains up to 1.1 [74] and in the wires drawn up to the strain of 1.5 [15, 21]. Detailed characterization [15] as described in Section 2.2 shows that this deviation has its origin in the initial macro-orientation of lamellae to the drawing direction. The calculated value is in good agreement with the experimental ones for the initial structure with the 0-30° lamellar orientation to the drawing direction, but underpredicts the ILS for the initial structure with the 30-90° lamellar orientation to

Please cite this paper as following: Xiaodan Zhang, Niels Hansen, Andrew Godfrey & Xiaoxu Huang (2018): Structure and strength of sub-100 nm lamellar structures in cold-drawn pearlitic steel wire, Materials Science and Technology
To link to this article: https://doi.org/10.1080/02670836.2018.1440155

the drawing direction. However, when all the measurements are combined with a fairly large standard error, it shows that an analysis based on the average measured values and calculation gives a reasonable description of the structural refinement with the increasing strain following equation (1). This indicates that for the quantification of the mean ILS a rather large area should be characterized covering the deformation microstructure from the different initial macro-orientations. However, it should also be noted that the initial microstructure and the chemical composition can also influence the refinement process of the ILS [75].

$$ILS = ILS_0 \exp(-\varepsilon/2) \quad (1)$$

Based on the edge-on conditions in the TEM [9, 11, 21], the evolution of the cementite thickness over a large area has been investigated and it has been found that this thickness decreases with the wire diameter up to the drawing strain of 3 in accordance with formula (1). As the strain is beyond 3, significant differences between the calculated and measured values appear, as shown in figure 12. These differences subdivided by the calculated thickness values point to the decomposition of 33%, 39% and 45% cementite with the release of carbon into the ferrite lamellae based on the original concentration of 3.63 at.% (0.8 wt.%) carbon.

The measured ILS, F and T are summarized in Table 2. It is interesting that at the highest strain the measured average cementite thickness is close to the critical edge length of a unit cell characterizing the original cementite (see figure 3) [76]. In parallel with the thinning of the cementite, cementite deforms to the limit and starts to break-down from the lamellar morphology to a plate-morphology with platelets distributed along the interface between neighboring ferrite lamellae (see figure 5). The limit of cementite deformation is also revealed as cementite lattices have been observed with only two layers of atoms. [11]

3.2 Dislocation density in ferrite lamellae

In the as-patented pearlite structure with 0.8 wt.% C, the ferrite occupies ~ 85 % of the volume fraction. It has been shown that the deformation of as-patented pearlite including yielding and flow is largely controlled by processes occurring in ferrite and that the role of a cementite lamellae is mainly to control the slip length of mobile dislocations which can be nucleated at ferrite - cementtie interfaces caused by elastic incompatibility stresses between the two phases [77-80]. Two specific types of dislocation sources have been observed via transmission electron microscopy in-situ straining experiments of thin foils with the observation area thickness 200 – 400 nm [81]: one dislocation source operates at wide interlamellar spacings of 250 – 300 nm by dislocation propagation in ferrite around cementite islands; the other consists of dislocations bulging in ferrite from interfaces and is more likely to operate at narrow interlamellar spacings of 50 nm. However, the actual dislocation processes during the drawing processes may be much more complicated taking into account the complex strain path [82], dynamic recovery introduced by the temperature increase during wire drawing [83], and contributions from other sources such as dislocation boundaries in the ferrite lamellae [11].

An alternative method to TEM is to analyze by X-ray the anisotropic peak broadening to obtain the dislocation density in the deformed microstructure. The two

Please cite this paper as following: Xiaodan Zhang, Niels Hansen, Andrew Godfrey & Xiaoxu Huang (2018): Structure and strength of sub-100 nm lamellar structures in cold-drawn pearlitic steel wire, Materials Science and Technology
To link to this article: https://doi.org/10.1080/02670836.2018.1440155

techniques are compared in Table 3, showing good agreement between the techniques at low and medium strains. At large strain there is a clear tendency that TEM gives higher values than X-ray for example at a strain of about 5, the numbers are 5.0×10^{16} m^{-2} (TEM) and 1.3×10^{16} m^{-2} (X-ray). This difference may have its cause in different patterns of stored dislocations. In TEM as shown in figure 13 and figure 14 dislocations are stored as threading dislocations and at high strains in cell boundaries, where the misorientation angle can be as high as 7.2º. In contrast, the X-ray estimations are based on the assumption that the deformation induced dislocations are organized randomly or are present in low angle dislocation boundaries. The dislocations in higher angle boundaries may not be accounted for by the X-ray technique.

The dislocation density determined by TEM and HREM is plotted in figure 15 as a function of the strain. The dislocation density increases with strain and the accumulation rate increases significantly when passing from the low strain region below about 2.5 to the high strain region 2.5 to 5.4. This transition is noteworthy as it may be related to another transition caused by decomposition of cementite to be discussed in the following section.

3.3 Carbon content in the ferrite lamellae

At medium and large strains, the carbon content in the ferrite lamellae is expected to increase as a consequence of cementite decomposition and release of carbon. Figure 16 summarizes the carbon content in the ferrite lamellae (versus the drawing strain) by different techniques: one dimensional atom probe field ion microscopy (1DAPFIM) [59, 76]; three dimensional atom probe tomography (3DAPT) [51]; calculation as a mass balance based on measured carbon concentration in cementite by 3DAPT [10]; calculation based on thinning of cementite lamellae [11]. The large spread may have its causes in both applied techniques and an inhomogeneous distribution of carbon atoms which affects the results obtained by local AP analysis. The large spread of the measured value (1DAPFIM and 3DAPT) comes from the fact that the distribution of carbon atoms in the ferrite lamellae from cementite decomposition is inhomogeneous with a gradient distribution from the ferrite/cementite interface to the interior of ferrite lamellae and a much higher concentration at dislocation boundaries, and the measured value normally concentrated close to the center of the ferrite lamellae and in the places between two neighboring dislocation boundaries in the ferrite lamellae where the carbon content is normally the lowest; while the calculated value from mass balance or extra thinning of cementite lamellae average the carbon content in the ferrite lamellae and minimize the effect of the inhomogeneous distribution of carbon atoms in the ferrite lamellae. However, all the results point to that above a strain between 2.5 and 3 the carbon content in the ferrite lamellae is significantly increased.

4. **Strengthening mechanisms**

Based on the structural observations and quantified structural parameters, the relationship between microstructure and strength has been analyzed by considering three strengthening mechanisms: boundary strengthening related to the distance between the cementite lamellae ($\sigma(b)$); dislocation strengthening related to the dislocation density in the ferrite lamellae ($\sigma(\rho)$); solid solution hardening related to the

Please cite this paper as following: Xiaodan Zhang, Niels Hansen, Andrew Godfrey & Xiaoxu Huang (2018): Structure and strength of sub-100 nm lamellar structures in cold-drawn pearlitic steel wire, Materials Science and Technology
To link to this article: https://doi.org/10.1080/02670836.2018.1440155

carbon concentration in the ferrite lamellae (σ (*ss*)). It is assumed that these strength contributions are linearly additive [86].

The contribution of cementite lamellae to the strength is estimated based on a Hall–Petch equation. In applying this equation to pearlite the barrier spacing is taken to be equal to the mean free path of dislocations, which is estimated to be twice the width of ferrite lamellae [8, 87]. This extrapolation from grain boundaries in polycrystalline structures to cementite lamellae in pearlitic structures is discussed by considering: the available volume for pile-ups' formation in the ferrite lamellae and the resistance to dislocation glide of cementite lamellae. Pile-ups have been analyzed in detail and the number of dislocations for a pile-up of edge or screw dislocations (n) has been related to the applied stress (σ)and the pile-up length (*Lp=2F*) [88]:

$$n = \pi Lp \cdot (\sigma / M) \cdot k / Gb \tag{2}$$

where k = 0.8 for an average between edge and screw dislocations and $M \approx 2$ for the <110> fiber texture, Eq. (5) can be written as:

$$n = 2.5 \cdot \frac{\sigma \cdot F}{Gb} \tag{3}$$

This calculation suggests the possible formation of a pile-up by 6 ~ 9 dislocations even in lamellae with the finest spacing by inserting the numbers where F equals the ferrite spacing in the range 70–11 nm, in agreement with the conclusion in a previous research where lower bound values were estimated for the grain sizes of different metals which can sustain a pile-up of two dislocations [89]. The thickness of cementite lamellae reduces with the wire diameter together with the decrease in interlamellar spacing during drawing, according to a power law $\varepsilon^{-0.5}$ relationship [9, 16]. The resistance of the cementite lamellae to dislocation glide may reduce due to thinning and decomposition. However, the resistance may also increase with strain due to the increase content of dislocations in the interfaces between cementite and ferrite lamellae as the misorientation across the lamellae with increased values show rotation of the ferrite lamellae around the wire axis (see figure 7).

The contribution of dislocation density to the strength of wires is estimated as forest hardening proportional to the square root of dislocation density. As an alternative to this mechanism, it has been suggested that the propagation of single dislocation loops in the volume between interfaces and the deposition of dislocations at or near the interface control the flow stress of fine laminated structures such as multilayers and drawn wires [90-92] with the possible controlling stress to propagate a dislocation and/or to push a dislocation through the interface. Inherent in this alternative mechanism is that dislocations are only stored not in the interior volume and at or near the interfaces. However, this is not the case in the present observations for drawn pearlitic wires, as dislocation cells form at the high strains and that the dislocation density is very high both in the ferrite lamellae and at the ferrite/cementite interface. The dislocations stored at the interfaces may also cause a stress on the cementite as a pile-up.

Solid solution hardening is introduced, as carbon enrichment of the ferrite is expected to lead to hardening due to the interaction between dislocations in different

Please cite this paper as following: Xiaodan Zhang, Niels Hansen, Andrew Godfrey & Xiaoxu Huang (2018): Structure and strength of sub-100 nm lamellar structures in cold-drawn pearlitic steel wire, Materials Science and Technology
To link to this article: https://doi.org/10.1080/02670836.2018.1440155

configurations and carbon atoms which are introduced through decomposition of cementite. Based on literature data, an average contribution from carbon in ferrite lamellae as a result of cementite decomposition has been estimated based on models by Krauss [93] and Winghall and Cohen [94]. Addition of strength contributions gives values for the flow stress $\sigma(\varepsilon)$ in good agreement with the experiments at low and medium strains, showing that the boundary strengthening and dislocation strengthening are the main contributors to the total flow stress (see Table 4).

However, at large strains beyond about 2.7, there is a clear tendency that the difference between the calculated and experimental flow stress can raise up to 12% at a strain of 5.4. This difference may have different causes where dislocation strengthening will be discussed in the following. This is because the contribution from σ (ρ) shows a very fast increase with increasing strain and as shown in Table 4 the contribution from dislocation strengthening and boundary strengthening are at the same magnitude at large strains. σ (ρ) is calculated as forest hardening equal to $M\alpha bG\sqrt{\rho}$ where the constant α relates to the free energy per unit-length of dislocation line and is proportional to *ln(R/b)* where *R* is the upper cut-off radius which decreases as the dislocation density increases [95]. α of 0.24 is used in the calculation but this value is derived from tensile-deformed specimens [96] where the dislocation density in these specimens is one to two orders of magnitude smaller than those in the drawn pearlitic steel wires, i.e., α = 0.24 may be an overestimation. Also the effect of dynamic recovery mechanisms has not been taken into account in the calculation. Such mechanism will reduce the flow stress but detailed mechanisms are at present unexplored. Such mechanisms can be dislocation – dislocation interaction and annihilation both in the ferrite and at the interface between ferrite and cementite. As shown for thermal recovery [97], the mechanisms will be affected by the presence of carbon atoms in solid solution which depends on the level of strain. The exploration of dynamic recovery is for upcoming research combining TEM, HREM and 3DAPT both in-situ and ex-situ [98].

5. Conclusions and Outlook

The microstructure and strengthening mechanisms in cold-drawn pearlitic steel wire (0.8 wt.% C) has been analysed with focus on the microstructural morphology and microstructural parameters in the strain range 0 - 5.4. The structural evolution is hierarchical with a transition range which may have its cause: decomposition of cementite releasing carbon atoms to the ferrite phase. The presence of a transition region suggests a separation of characterization and analysis into three strain ranges 0 – 2.7 (low/medium), 2.7 – 5.4 (transition), 5.4 – 7.0 (maximum). The present paper is an overview with focus on the first two ranges encompassing at a strain of 5.4 a reduction in the lamellar spacing to 10 nm and an increase in dislocation density to 5×10^{16} m^{-2}. Three strengthening mechanisms are considered: (i) Hall-Petch strengthening; (ii) dislocation strengthening; (iii) solid solution hardening; and all contributions appear to increase with increasing strain. Noteworthy is that the contributions from Hall-Petch strengthening and dislocation strengthening have increased to the same level at a strain of 5.4 and that saturation is not observed. This points to future research including parameters supplementary to the strain, for example, process parameters and addition of alloying elements. The scale of the structure is expected to reach below 10 nm and the characterization techniques must be further developed. A first step will be a

Please cite this paper as following: Xiaodan Zhang, Niels Hansen, Andrew Godfrey & Xiaoxu Huang (2018): Structure and strength of sub-100 nm lamellar structures in cold-drawn pearlitic steel wire, Materials Science and Technology
To link to this article: https://doi.org/10.1080/02670836.2018.1440155

combination of transmission electron microscopy, high resolution electron microscopy and three dimensional atom probe tomography where themes are strengthening mechanisms including the effect of thermal and dynamic recovery. Also the information acquired and the methodology applied in the present review on the analysis of microstructure and strengthening mechanisms can also be the basis for an analysis of nanometer-scale lamellar structures produced by other techniques, such as cold rolling [49, 99], equal channel angular pressing [100], high pressure torsion [101-104] and low temperature annealing [105-108], and further themes on such as hydrogen embrittlement resistance [105] and anisotropy in the mechanical properties including delamination and fracture toughness [109].

References

1. National Research Council. Materials and Man's Needs: Materials Science and Engineering -- Volume I, The History, Scope, and Nature of Materials Science and Engineering. Washington, DC: The National Academies Press; 1975.
2. Tsuji N, Maki T. Enhanced structural refinement by combination phase transformation and plastic deformation in steels. Scripta Mater. 2009;60:1044-1049.
3. Christian JW. The Theory of Transformations in Metals and Alloys. 2002. Pergamon.
4. Bhadeshia HKDH. Nanostructured bainite. Proc R Soc A. 2010;466:3-18.
5. Percy J. On steel wire of high tenacity. J Iron Steel Inst. 1886;29:62-80.
6. Tarui T, Maruyama N, Takahashi J, et al. Microstructure control and strengthening of high-carbon steel wires. Nippon Technical Report. 2005;91:56-61.
7. Li Y, Raabe D, Herbig M, et al. Segregation stabilizes nanocrystalline bulk steel with near theoretical strength. Phys Rev Lett. 2014;113:106104.
8. Embury JD, Fisher RM. The structure and properties of drawn pearlite. Acta Metall. 1966;14:147-159.
9. Zhang X, Godfrey A, Huang X, et al. Microstructure and strengthening mechanisms in cold-drawn pearlitic steel wire. Acta Mater. 2011;59:3422-3430.
10. Li YJ, Choi P, Borchers C, et al. Atomic-scale mechanisms of deformation-induced cementite decomposition in pearlite. Acta mater. 2011;59:3965-3977.
11. Zhang X, Hansen N, Godfrey A, et al. Dislocation-based plasticity and strengthening mechanisms in sub-20 nm lamellar structures in pearlitic steel wire. Acta mater. 2016;114:176-183.
12. Borchers C, Kirchheim R. Cold-drawn pearlitic steel wires. Prog Mater Sci. 2016; 82:405-444.
13. Zubov VY. Patenting of steel wire. Met Sci Heat Treat. 1972;14:793–800.
14. Redley N. A review of the data on the interlamellar spacing of pearlite. Metall Trans. 1984;15A:1019-1036.
15. Zhang X, Godfrey A, Hansen N, et al. Hierarchical structures in cold-drawn pearlitic steel wire Acta Mater. 2013;61:4898–4909.
16. Zhang X. Quantitative investigation of microstructural evolution during the cold wire-drawing of a pearlitic steel wire and its relationship with mechanical properties. PhD thesis. 2009. Tsinghua Univ. Beijing.
17. Langford G. A study of the deformation of patented steel wire. Metall Trans. 1970; 1:465-477.

Please cite this paper as following: Xiaodan Zhang, Niels Hansen, Andrew Godfrey & Xiaoxu Huang (2018): Structure and strength of sub-100 nm lamellar structures in cold-drawn pearlitic steel wire, Materials Science and Technology
To link to this article: https://doi.org/10.1080/02670836.2018.1440155

18. Langford G. Deformation of pearlite. Metall Trans. 1977;8A:861-875.
19. Zelin M. Microstructure evolution in pearlitic steels during wire drawing. Acta Mater. 2002;50:4431-4447.
20. Zhang XD, Godfrey A, Huang X, et al. Characterization of the microstructure in drawn pearlitic steel wires. Proceedings of the 30th Risø International Symposium on Materials Science: Nanostructured Metals: Fundamentals to Applications. Risø, Denmark: DTU. 2009. pp. 409-416.
21. Zhang X, A. Godfrey, N. Hansen, X. Huang, W. Liu and Q. Liu: 'Evolution of cementite morphology in pearlitic steel wire during wet wire drawing' Mater. Charact., 2010, 61, 65-72.
22. X.D. Zhang, Godfrey A, Liu W, et al. Study on dislocation slips in ferrite and deformation of cementite in cold drawn pearlitic steel wires from medium to high strain. Mater Sci Technol. 2011;27:562-567.
23. Zhang X, Hansen N, Godfrey A, et al. Microstructural evolution, strengthening mechanisms and strength structure relationship in cold-drawn pearlitic steel wire. Proceedings of the 33rd Risø International Symposium on Materials Science: Nanometals: Status and Perspectives. Risø, Denmark. 2012. pp. 407-416.
24. Zhang X, Hansen N, Godfrey A, et al. Hierarchical structures and strength in cold-drawn pearlitic steel wire. Proceedings of the 35rd Risø International Symposium on Materials Science: New Frontiers of Nanometals. Risø, Denmark. 2014. pp. 153-160.
25. Guo N, Luan B, Wang B, et al. Microstructure and texture evolution in fully pearlitic steel during wire drawing. Sci China tech Sci. 2013;56:1139-1146.
26. Zhou L, Hu X, Ma C, et al. Effect of pearlitic lamella orientation on deformation of pearlite steel wire during cold drawing. Acta Metall Sin. 2015;51:897-903.
27. Kumar P, Gurao NP, Haldar A, et al. Progressive changes in the microstructure and texture in pearlitic steel during wire drawing. ISIJ International. 2011;51:679-684.
28. Zhao T, Zhang G, Zhang S, et al. Influence of lamellar direction in pearlitic steel wire on mechanical properties and microstructure evolution. J Iron Steel Res Int. 2016;23:1290-1296.
29. Toribio J, Ovejero E. Microstructure evolution in a pearlitic steel subjected to progressive plastic deformation. Mater Sci Eng A. 1997;234-236:579-582.
30. Hosford WF. Microstructural changes during deformation of [110] fiber textured metals. Trans Met Soc AIME. 1964;230:12-15.
31. Aernoudt E, Van Houtte P, Leffers T. Deformation and textures of metals at large strain. Plastic Deformation and Fracture of Materials. VCH, Weinheim, Newyork; Basel; Cambridge. 1993. pp. 129.
32. Gil Sevillano J. Large strain work hardening and textures. Prog Mater Sci. 1981;25: 69-134.
33. Shein IR, Medvedeva NI, Ivanovskii AL. Electronic and structural properties of cementite-type M3X (M = Fe, Co, Ni; X = C or B) by first principles calculations. Physica B. 2006;371:126-132.
34. Puttick KE. Structure, deformation, and fracture of pearlite. J Iron Steel Inst. 1957; 185:161-176.
35. Park J, Kim S-D, Hong S-P, et al. Quantitative measurement of cementite dissociation in drawn pearlitic steel. Mater Sci Eng A. 2011;528:4947-4952.
36. Fang F, Zhao Y, Liu P, et al. Deformation of cementite in cold drawn pearlitic steel wire. Mater Sci Eng A. 2014;608:11-15.

Please cite this paper as following: Xiaodan Zhang, Niels Hansen, Andrew Godfrey & Xiaoxu Huang (2018): Structure and strength of sub-100 nm lamellar structures in cold-drawn pearlitic steel wire, Materials Science and Technology
To link to this article: https://doi.org/10.1080/02670836.2018.1440155

37. Keh AS. Imperfections and plastic deformation of cementite in steel. Acta Metall. 1963;11:1101-1103.
38. Nishiyama Z, Kore'eda A, Katagiri S. Study of plane defects in the cementite by transmission electron microscopy. Trans JIM. 1964;5:115-121.
39. Maurer K, Warrington DH. Deformation of cementation. Phil Mag. 1967;15:321-327.
40. Koréeda A, Shimizu K. Dislocations in cementite. Phil Mag. 1968;17:1083-1086.
41. Gil Sevillano J. Room temperature plastic deformation of pearlitic cementite. Mater Sci Eng. 1975;21:221-225.
42. Karlsson B, Lindén G. Plastic deformation of eutectoid steel with different cementite morphologies. Mater Sci Eng, 1975;17:153-164.
43. Karlsson B, Lindén G. Plastic deformation of ferrite - pearlite structures in steel. Mater Sci Eng. 1975;17:209-219.
44. Inoue A, Ogura T, Masumoto T. Burgers vectors of dislocations in cementite crystal. Scripta Mater. 1977;11:1-5.
45. Inoue A, Ogura T, Masumoto T. Microstructure of deformation and fracture of cementitie in pearlite carbon steels strained at various temperatures. Metall Trans A. 1977;8:1689-1695.
46. Kar'kina LE, Zubkova TA, Yakovleva IL. Dislocation structure of cementite in granular peartlite after cold plastic deformation. Phys Met Metallogr. 2013;114:234-241.
47. Taniyama A, Takayama T, Arai M, et al. Deformation behavior of cementite in deformed high carbon steel observed by X-ray diffraction with synchrotron radiation. Metall Mater Trans A. 2017;48:4821-4830.
48. Porter DA, Easterling KE. Dynamic studies of the tensile deformation and fracture of pearlite. Acta Metall. 1978;26:1405-1422.
49. Tagashira S, Sakai K, Furuhara T, et al. Deformation Microstructure and Tensile Strength of Cold Rolled Pearlitic Steel Sheets. ISIJ Int. 2000;40:1149-1156.
50. Borchers C, Al-Kassab T, Goto S, et al. Partially amorphous nanocomposite obtained from heavily deformed pearlitic steel. Mater Sci Eng A. 2009;25:131-138.
51. Hong MH, Reynolds WT, Tarui T, et al. Atom probe and transmission electron microscopy investigations of heavily drawn pearlitic steel wire. Metall Mat Trans A. 1999;30:717-727.
52. Goto S, Kirchheim R, Al-Kassab T, et al. Application of cold drawn lamellar microstructure for developing ultra-high strength wires Trans Nonferrous Met Soc China. 2007;17:1129-1138.
53. Xu B, Zhang X. Understanding twinning nucleation and dislocation core structure through interscale hybrid methods. Proceedings of the 35th Risø international symposium on materials science: New frontiers of nanometals. 2014. Risø, Denmark.
54. Gridnev VN, Gavrilyuk VG, Dekhtyar IY, et al. Investigation of carbide phase in strained steel by the method of nuclear gamma resonance. Phys Status Solidi A. 1972;14:689-694.
55. Gavriljuk VG. Decomposition of cementite in pearlitic steel due to plastic deformation. Mater Sci Eng A. 2003;345:81-89.

Please cite this paper as following: Xiaodan Zhang, Niels Hansen, Andrew Godfrey & Xiaoxu Huang (2018): Structure and strength of sub-100 nm lamellar structures in cold-drawn pearlitic steel wire, Materials Science and Technology
To link to this article: https://doi.org/10.1080/02670836.2018.1440155

56. Nam WJ, Bae CM, Oh SJ, et al. Effect of interlamellar spacing on cementite decomposition during wire drawing of pearlitic steel wires. Scripta Mater. 2000;42: 457-463.
57. Ivanisenko Y, Lojkowski W, Valiev RZ, et al. The mechanism of formation of nanostructure and decomposition of cementite in a pearlitic steel during high pressure torsion. Acta Mater. 2003;51:5555-5570.
58. Languillaume J, Kapelski G, Baudelet B. Cementite decomposition in heavily cold drawn pearlitic steel wires. Acta Mater. 1997;45:1201-1212.
59. Read HG, Reynolds WT, Hono K, et al. APFIM and TEM studies of drawn pearlitic wire. Scr. Mater. 1997;37:1221-1230.
60. Hono K, Ohnuma M, Murayama M, et al. Cementite decomposition in heavily drawn pearlite steel wire. Scripta Mater. 2001;44:977-983.
61. Takahashi J, Tarui T, Kawakami K. Three-dimensional atom probe analysis of heavily drawn steel wires by probing perpendicular to the pearlitic lamellae. Ultramicroscopy. 2009;109:193-199.
62. Sauvage X, Lefebvre W, Genevois C, et al. Complementary use of transmission electron microscopy and atom probe tomography for the investigation of steels nanostructured by severe plastic deformation. Scr Mater. 2009;60:1056-1061.
63. Jiang C, Srinivasan SG, Caro A, et al. Structural, elastic, and electronic properties of Fe3C from first principles. J Appl Phys. 2008;103:043502.
64. Voronin VI, Berger IF, Gornostyrev YN, et al. Composition of cementite in the dependence on the temperature. In situ neutron diffraction study and ab initio calculations. JETP Lett. 2010;91:143-146.
65. Zhang X, Godfrey A, Liu W, et al. Evolutions of microstructure and ferritic micro-orientation and texture in a pearlitic steel wire during cold drawing. Acta Metall Sin. 2010;46:141-146.
66. Zidani M, Messaoudi S, Baudin T, et al. Deformation textures in wire drawn pearlitic steel. Int J Mater Form. 2010;3:7-11.
67. Yang F, Ma C, Jiang JQ, et al. Effect of cumulative strain on texture characteristics during wire drawing of eutectoid steels. Scripta Mater. 2008;59:850-853.
68. Heizmann JJ, Tidu A, Bolle B, et al. Influence of the crystallographic texture on the torsional behavior of steel cord. Wire J Int. 1999;32:150-158.
69. Liu Y, Jiang QW, Wang G, et al. Influence of microstructures and textures on the torsional behavior of pearlitic wires. J Mater Sci Technol. 2005;21:357-360.
70. Abdellaoui A, Montesin T, Heizmann JJ, et al. Study on the texture of steelcord during the wet drawing process: influence of the patenting and the friction on the dies. Mater Sci Forum. 1994;157-162:611-616.
71. Montesin T, Heizmann JJ. Evolution of crystallographic texture in thin wires. J Appl Cryst. 1992;25:665-673.
72. Van Houte P, Watté P, Aernoudt E, et al. Taylor simulation of cyclic textures at the surfae of drawn wires using a simple flow field model. 1994;157-162:1881-1886.
73. Zhao T-Z, Zhang G-L, Song H-W, et al. Crystallographic texture difference between center and sub-surface of thin cold-drawn pearlitic steel wires. J Mater Eng Perform. 2014;23:3279-3284.
74. Toribio J, Ovejero E. Effect of cumulative cold drawing on the pearlite interlamellar spacing in eutectoid steel. Scripta Mater. 1998;39:323-328.

Please cite this paper as following: Xiaodan Zhang, Niels Hansen, Andrew Godfrey & Xiaoxu Huang (2018): Structure and strength of sub-100 nm lamellar structures in cold-drawn pearlitic steel wire, Materials Science and Technology
To link to this article: https://doi.org/10.1080/02670836.2018.1440155

75. Park J, Kim S-D, Hong S-P, et al. Quantitative measurement of cementite dissociation in drawn pearlitic steel. Mater Sci Eng A. 2011;528:4947-4952.
76. Maruyama N, Tarui T, Tashiro H. Atom probe study on the ductility of drawn pearlitic steels. Scr Mater. 2002;46:599-603.
77. Dollar M, Bernstein IM, Thompson AW. Influence of deformation substructure on flow and fracture of fully pearlitic steel. Acta Metall. 1988;36:311-320.
78. Hackney SA, Shiflet GJ. Anisotropy interfacial energy at pearlite lamellar boundaries in a high purity Fe - 0.80 % C alloy. Scripta Metall. 1986;20:389-394.
79. Zhou DS, Shiflet GJ. Ferrite: cementite crystallography in pearlite. Metall Trans. 1992;23A:1259-1269.
80. Kim J, Kang K, Ryu S. Characterization of the misfit dislocations at the ferrite/cementite interface in pearlitic steel: an atomistic simulation study. Int J Plasticity. 2016;83:302-312.
81. Janecek M, Louchet F, Doisneau-Cottignies B, et al. Specific dislocation multiplication mechanisms and mechanical properties in nanoscaled multilayers: the example of pearlite. Phil Mag A. 2000;80:1605-1619.
82. Zhao T-Z, Song H-W, Zhang S-H. Non-monotonic radial distribution of tensile yielding strength in cold-drawn pearlitic wire. Mater Sci Technol. 2017, doi:10.1080/02670836.2017.1352642.
83. Langford G, Cohen M, Strain hardening of iron by severe plastic deformation. Trans ASM, 1969;62:623.
84. Chakraborty J, Ghosh M, Ranjan R, et al. X-ray diffraction and mössbauer spectroscopy studies of cementite decomposition in cold-drawn pearlitic steel. Phil Mag. 2013;93:4598-4616.
85. Chen YZ, Csiszár G, Cizek J, et al. Defects in carbon-rich ferrite of cold-drawn pearlitic steel wires. Metall Mater Trans A. 2013;44:3882-3889.
86. Hughes DA, Hansen N. Microstructure and strength of nickel at large strains. Acta mater. 2000;48:2985-3004.
87. Gensamer M, Pearsall EB, Pellini WS, et al. Tensile properties of steel. Trans ASM. 1942;30:983-1019.
88. Eshelby JD, Frank FC, Nabarro FRN. The equilibrium of linear arrays of dislocations. Phil Mag. 1951;42:351-364.
89. Nieh TG, Wadsworth J. Hall-petch relation in nanocrystalline solids. Scripta Metall Mater. 1991;25:955-958.
90. Embury JD, Hirth JP. On dislocation storage and the mechanical response of fine scale microstructures. Acta Metall Mater. 1992;42:2051-2056.
91. Gil Sevillano J. Substructure and strengthening of heavily deformed single and two-phase metallic materials. J Phys III. 1991;1:967-988.
92. Misra A, Kung H, Embury JD. Preface to the viewpoint set on: deformation and stability of nanoscale metallic multilayers. Scripta Mater. 2004;50:707-710.
93. Krauss G. Martensite in steel: strength and structure. Mater Sci Eng A. 1999;273-275:40.
94. Winghell PG, Cohen M. Solid-solution strengthening of martensite by carbon. Electron Microscopy and Strength of Crystals. Interscience Publishers, New York. 1963. p.995.
95. Kuhlmann-Wilsdorf D. Strengthening through LEDS, Strength of Metals and Alloys (ICSMA 8), 1989, Vol. 1, P221-226.

Please cite this paper as following: Xiaodan Zhang, Niels Hansen, Andrew Godfrey & Xiaoxu Huang (2018): Structure and strength of sub-100 nm lamellar structures in cold-drawn pearlitic steel wire, Materials Science and Technology
To link to this article: https://doi.org/10.1080/02670836.2018.1440155

96. Hansen N, Huang X. Microstructure and flow stress of polycrystals and single crystals. Acta Mater. 1998;46:1827-1836.
97. Hirakami D, Ushioda K, Manabe T, et al. Change in the microstructure and mechanical properties of drawn pearlitic steel with low-temperature aging. Proceedings of the 38th Risø International Symposium on Materials Science: Advanced Metallic Materials by Microstructural Design. Risø, Denmark. 2017. pp. 259-266.
98. Herbig M, Choi P, Raabe D. Combining structural and chemical information at the nanometerscale by correlative transmission electron microscopy and atom probe tomography. Ultramicroscopy. 2015;153:32-39.
99. Lv ZQ, Jiang P, Wang ZH, et al. XRD analyses on decomposition behavior of cementite in eutectoid pearlitic steel during cold rolling. Mater Lett. 2008;62:2825-2827.
100. Wetcher F, Stock R, Pippan R. Changes in the mechanical properties of a pearlitic steel due to large shear deformation. Mater Sci Eng A. 2007;445:237-243.
101. Ivanisenko Y, Lojowski W, Valiev RZ, et al. The mechanism of formation of nanostructure and decomposition of cementite in a pearlitic steel during high pressure torsion. Acta Mater. 2003;51:5555-5570.
102. Wetscher F, Pippan R, Sturm S, et al. TEM investigations of the structural evolution in a pearlitic steel deformed by high-pressure torsion. Metall Mater Trans A. 2006;37:1963-1968.
103. Sauvage X, Ivanisenko Y. The role of carbon segregation on nanocrystallisation of pearlitic steels processed by severe plastic deformation. J Mater Sci. 2007;42: 1615-1621.
104. Hohenwarter A, Taylor A, Stock R, et al. Effect of large shear deformations on the fracture behavior of a fully pearlitic steel. Metall Mater Trans A. 2011;42:1609-1618.
105. Hirakami D, Ushioda K, Manabe1 T, et al. Change in the microstructure and mechanical property of drawn pearlitic steel with low-temperature aging. IOP Conference Series: Materials Science and Engineering, 2017;219:012026.
106. Buono VTL, Andrade MS, Gonzalez BM. Kinetics of strain aging in drawn pearlitic steels. Metall Mater Trans A. 1998;29:1415-1423.
107. Watté P, Van Humbeeck J, Aernoudt E, et al. Strain ageing in heavily drawn eutectoid steel wires. Scr. Mater. 1996;34:89-95.
108. Zhang X, Bech JI, Hansen N. Low temperature annealing of cold-drawn pearlitic steel wire. IOP Conference Series: Materials Science and Engineering. 2015;89:012158.
109. Hohenwarter A, Völker B, Kapp MW, et al. Ultra-strong and damage tolerant metallic bulk materials: A lesson from nanostructured pearlitic steel wires. Sci rep. 2016;6:33228.

Please cite this paper as following: Xiaodan Zhang, Niels Hansen, Andrew Godfrey & Xiaoxu Huang (2018): Structure and strength of sub-100 nm lamellar structures in cold-drawn pearlitic steel wire, Materials Science and Technology
To link to this article: https://doi.org/10.1080/02670836.2018.1440155

Table 1. Definition of microstructures at different strains [15, 21]

Microstructure type	Strain	Description
Type I	0 ~ 2.7	angle between the length direction of the cementite plates and the wire axis: 0° – 30°
Type II	0 ~ 2.7	angle between the length direction of the cementite plates and the wire axis: 30° – 60°
Type III	0 ~ 2.7	angle between the length direction of the cementite plates and the wire axis: 60° – 90°
A, B and C	0	angle between the length direction of the cementite plates and the wire axis: 0° – 30°, 30° – 60° and 60° – 90°
A_A, A_B and A_C	$0 < \varepsilon \leq 1.5$	deformation structures which have their origins in A, B and C colonies in the patented wire
A_A and A_BC	$1.5 < \varepsilon \leq 3.7$	deformation structures which have their origins in A and (B and C) colonies in the patented wire (see text)

Table 2. Measured ILS, F and T up to the strain of 5.4 [Reprinted from ref 9 and ref 11, with permission from Elsevier]

	Strain						
	0	0.7	1.5	2.7	3.7	4.2	5.4
ILS (nm)	89	70	55	28	20	15.4	11.7
F (nm)	70	56	45	23	18	14	11
T (nm)	19	14	10	5	2	1.4	0.7

Table 3. Measured dislocation density in the ferrite

Technique	Strain	Dislocation density (m^{-2})	Chemical composition (wt.%)
TEM	0	7.0×10^{13}	0.80 C [9]
	0.7	7.0×10^{14}	0.80 C [9]
	1.5	2.0×10^{15}	0.80 C [9]
	2.7	8.8×10^{15}	0.80 C [9]
	3.7	2.0×10^{16}	0.80 C [9]
	4.2	2.8×10^{16}	0.80 C [11]
	5.4	5.0×10^{16}	0.80 C [11]
X-ray	0.12	6.0×10^{14}	0.80 C [84]
	1.4	8.0×10^{15}	0.80 C [84]

Please cite this paper as following: Xiaodan Zhang, Niels Hansen, Andrew Godfrey & Xiaoxu Huang (2018): Structure and strength of sub-100 nm lamellar structures in cold-drawn pearlitic steel wire, Materials Science and Technology
To link to this article: https://doi.org/10.1080/02670836.2018.1440155

	0	8.0×10^{14}	0.82 C [85]
	1	3.8×10^{15}	0.82 C [85]
	2	4.8×10^{15}	0.82 C [85]
	3	8.0×10^{15}	0.82 C [85]
	4	1.2×10^{16}	0.82 C [85]
	5	1.3×10^{16}	0.82 C [85]

Table 4. Calculated and measured flow stress in the range 0-5.4 [Reprinted from ref 11, with permission from Elsevier]

	Strain						
	0	0.7	1.5	2.7	3.7	4.2	5.4
$\sigma(b)$(MPa)	829	926	1033	1445	1634	1853	2090
$\sigma(\rho)$(MPa)	77	244	569	865	1305	1544	2063
$\sigma(ss)$(MPa)	~0	~0	~0	~0	744	794	829
σ_0(MPa)	60	60	60	60	60	60	60
σ_{cal}(MPa)	966	1230	1662	2370	3743	4251	5042
σ_{exp}(MPa)*	880	1286	1614	2365	3395	3887	4510
Diff.(MPa)	86	-56	48	5	338 (10%)	364 (9%)	532 (12%)

*0.2% proof stress

Please cite this paper as following: Xiaodan Zhang, Niels Hansen, Andrew Godfrey & Xiaoxu Huang (2018): Structure and strength of sub-100 nm lamellar structures in cold-drawn pearlitic steel wire, Materials Science and Technology
To link to this article: https://doi.org/10.1080/02670836.2018.1440155

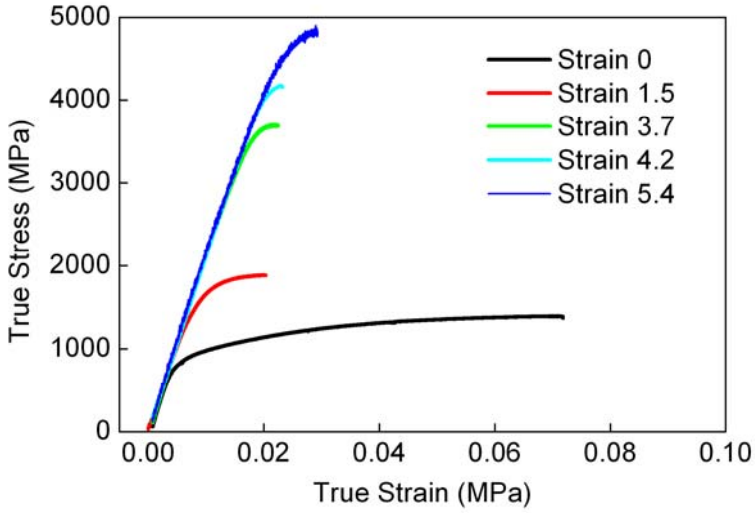

Figure 1. True stress-true strain tensile curves for the wires showing parabolic work hardening and no yield point [Reprinted from ref 9 and ref 11, with permission from Elsevier].

Please cite this paper as following: Xiaodan Zhang, Niels Hansen, Andrew Godfrey & Xiaoxu Huang (2018): Structure and strength of sub-100 nm lamellar structures in cold-drawn pearlitic steel wire, Materials Science and Technology
To link to this article: https://doi.org/10.1080/02670836.2018.1440155

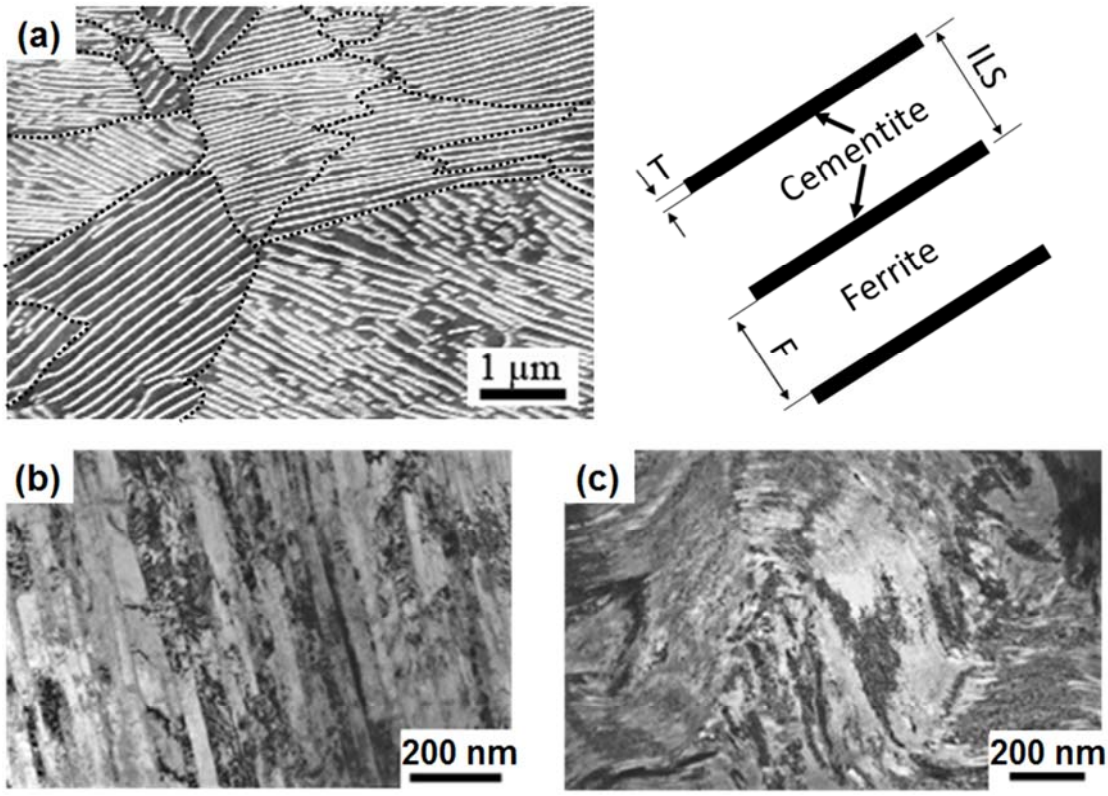

Figure 2. Microstructure of 0.8 wt.% C pearlitic steel wires before and after drawing: (a) SEM image of the pearlitic microstructure with a sketch to show the structural parameters in the initial as-patented wire and TEM images of the microstructure in the (b) longitudinal section and (c) cross section of a wire at a strain of 3.7. The pearlite colony boundaries are marked with black dashed lines. ILS, T and F in the sketch showing the edge-on condition of lamellar structure represent interlamellar spacing, the thickness of cementite and the thickness of ferrite, respectively. The sum of F and T equals to ILS.

Please cite this paper as following: Xiaodan Zhang, Niels Hansen, Andrew Godfrey & Xiaoxu Huang (2018): Structure and strength of sub-100 nm lamellar structures in cold-drawn pearlitic steel wire, Materials Science and Technology
To link to this article: https://doi.org/10.1080/02670836.2018.1440155

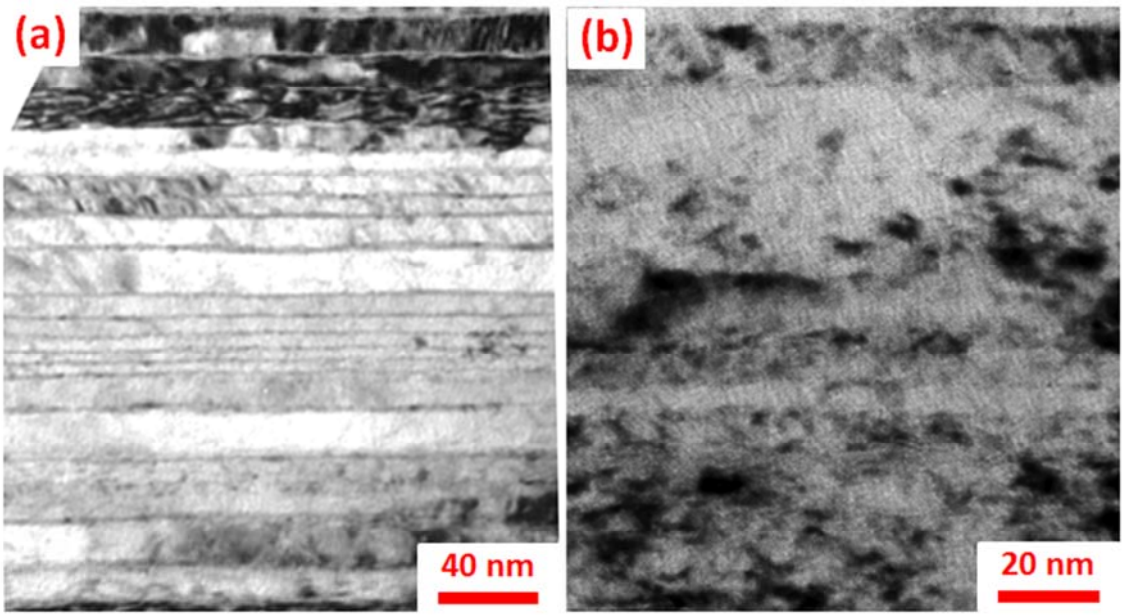

Figure 3. TEM micrographs show the microstructure at strains of 4.2 and 5.4. The drawing direction is horizontal, parallel to the lamellar direction. The morphology changes from an almost continuous cementite lamellae separating ferrite lamellae in (a) to cementite platelets distributed along the interface between neighboring ferrite lamellae in (b). These platelets are irregular in shapes and oriented parallel to the drawing direction. [Reprinted from ref 11, with permission from Elsevier]

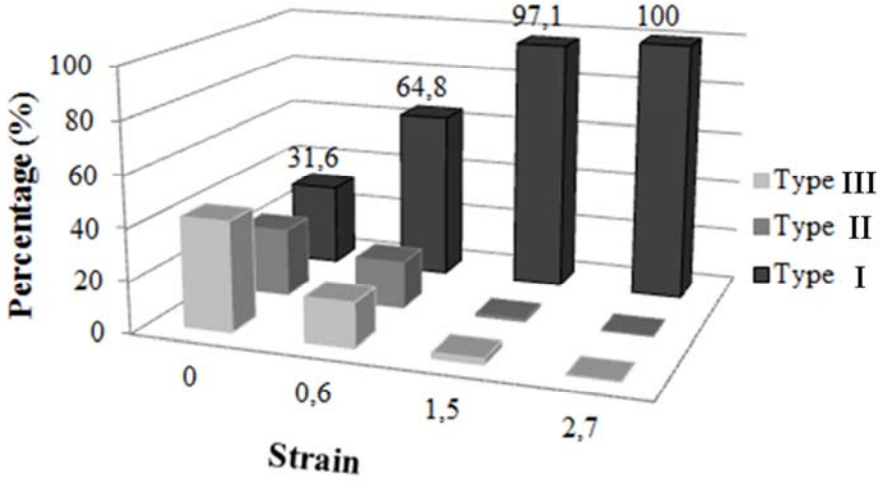

Figure 4. Bar chart summarizing the data for the alignment in the longitudinal section of the cementite plates/particles as a function of drawing strain. Percentages are given as determined from area fractions. This figure illustrates the reorientation of cementite to be parallel to the drawing direction at a strain of 2.7 and above.

Please cite this paper as following: Xiaodan Zhang, Niels Hansen, Andrew Godfrey & Xiaoxu Huang (2018): Structure and strength of sub-100 nm lamellar structures in cold-drawn pearlitic steel wire, Materials Science and Technology
To link to this article: https://doi.org/10.1080/02670836.2018.1440155

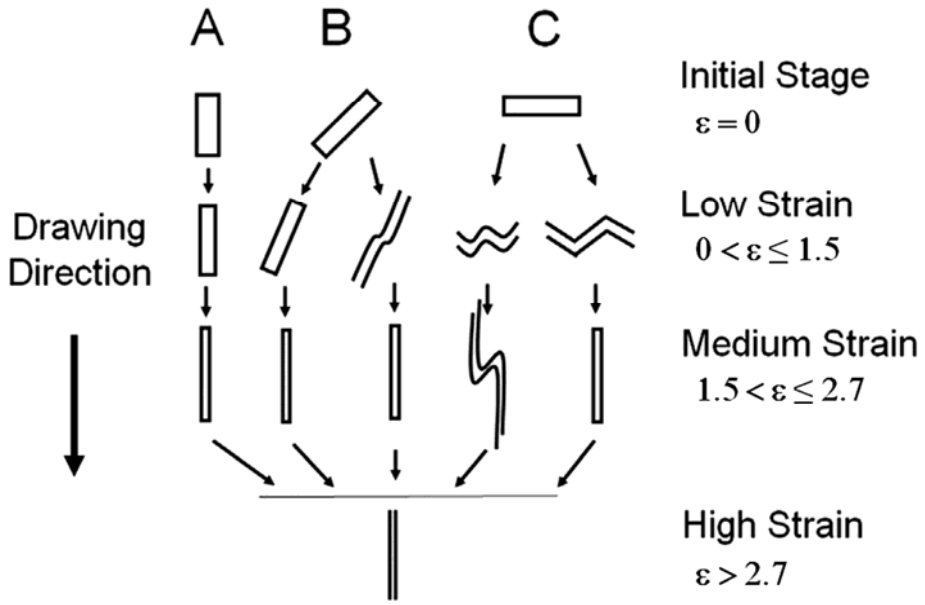

Figure 5. Schematic illustration of five evolutionary paths for changes in the macroscopic alignment, morphology and thickness of ferrite lamellae in the longitudinal section with cold drawing from low to high strain (see text) [Reprinted from ref 15, with permission from Elsevier].

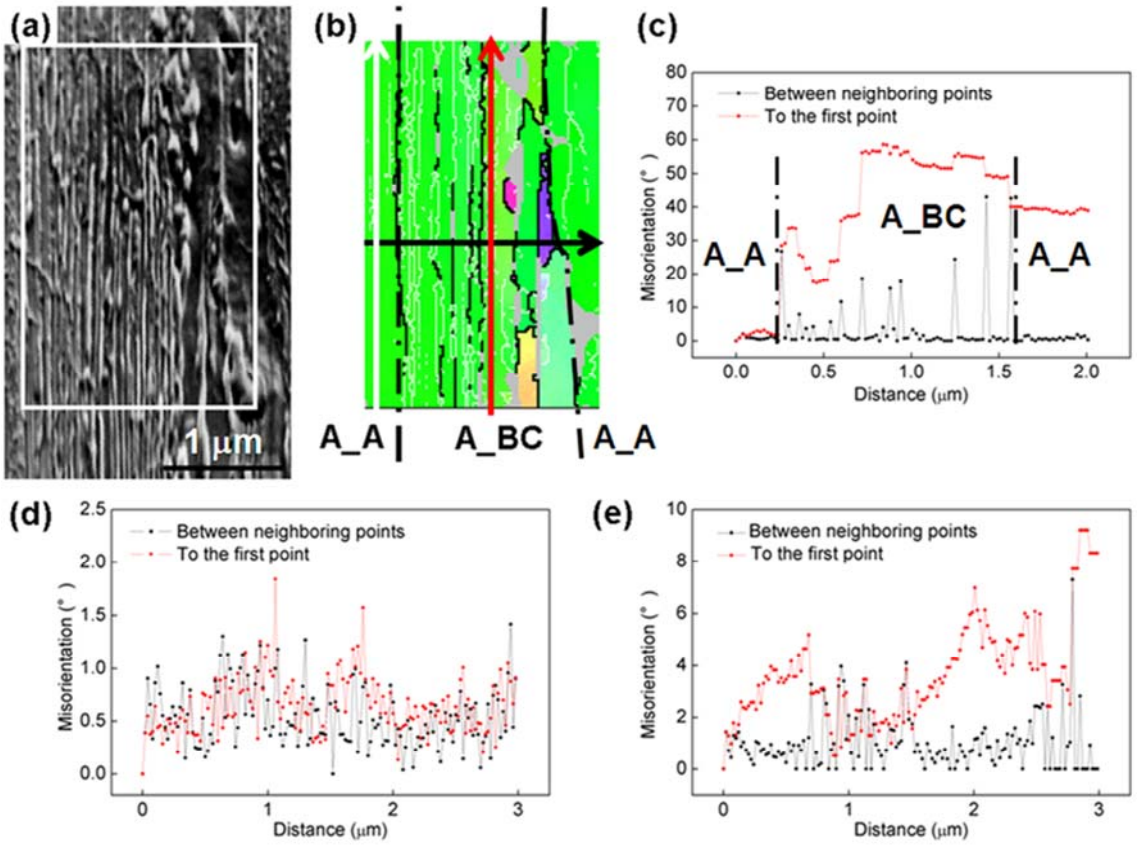

Please cite this paper as following: Xiaodan Zhang, Niels Hansen, Andrew Godfrey & Xiaoxu Huang (2018): Structure and strength of sub-100 nm lamellar structures in cold-drawn pearlitic steel wire, Materials Science and Technology
To link to this article: https://doi.org/10.1080/02670836.2018.1440155

Figure 6. Image (a) and EBSD map (b) in Inverse Pole Figure (IPF) coloring. The arrows (black, white and red) mark positions for orientation angle measurements across and along the ferrite lamellae at a strain of 2.7. Angular changes across the lamellae (black arrow) are shown in (c); Angular changes along the lamellae (white and red arrows) are shown in (d) and (e) for A_A and A_BC structures, respectively. The black dashed lines in (b) show the interfaces between A_A and A_BC structure (see text) [Reprinted from ref 15, with permission from Elsevier].

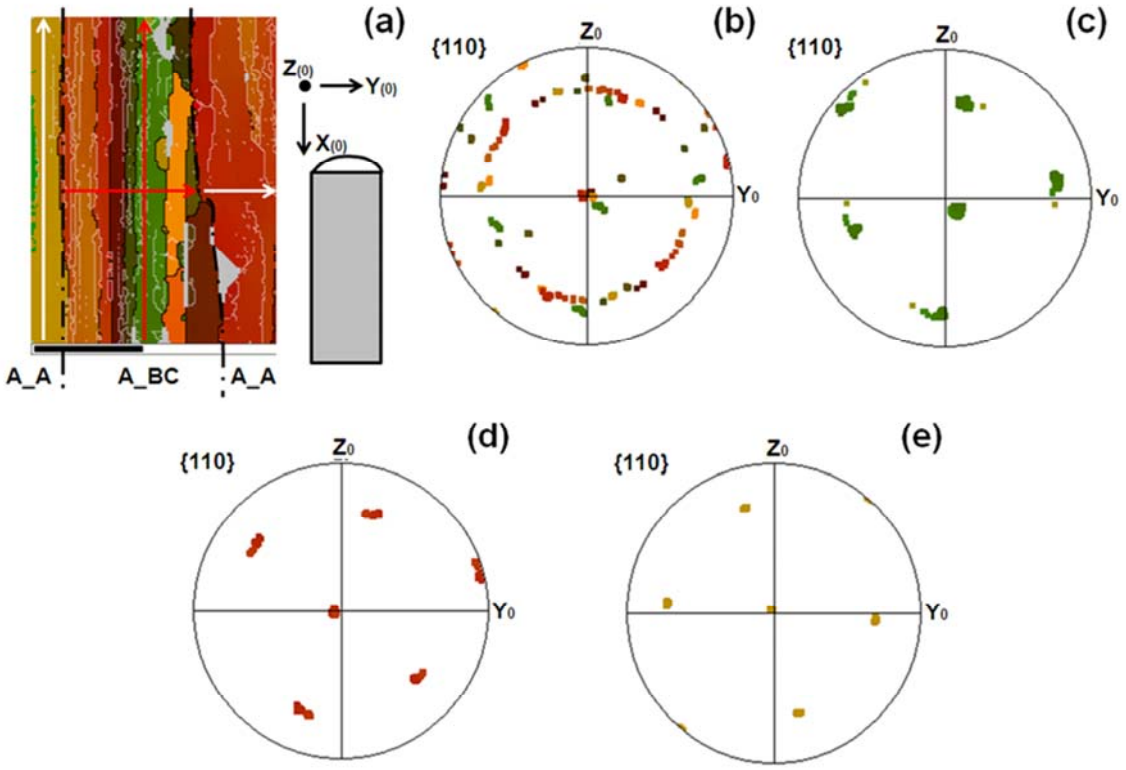

Figure 7. EBSD map in all Euler coloring using the same data set as in figure 4b with a schematic illustrating the coordinate set in a central longitudinal section (a); and {110} pole figures showing the crystal rotation in the A_BC structure across (b) and along (c) lamellae (red arrows), and in the A_A structure across (d) and along (e) lamellae (white arrows). The strain of the sample is 2.7.

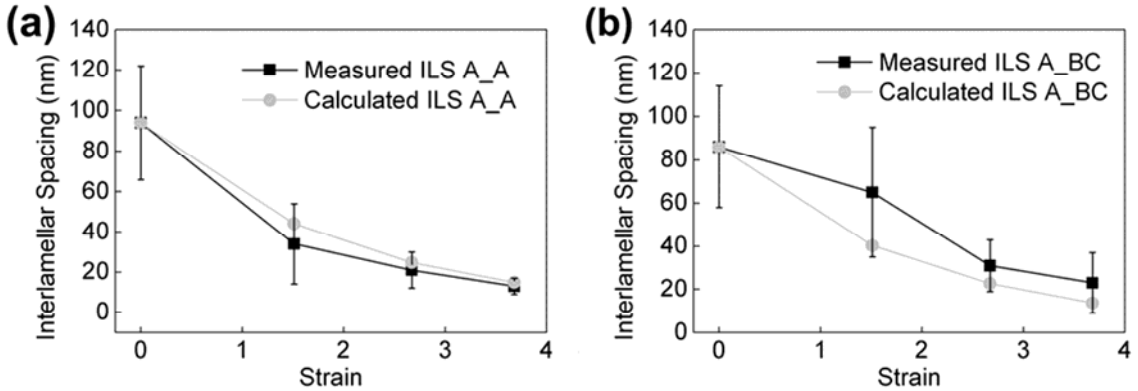

Please cite this paper as following: Xiaodan Zhang, Niels Hansen, Andrew Godfrey & Xiaoxu Huang (2018): Structure and strength of sub-100 nm lamellar structures in cold-drawn pearlitic steel wire, Materials Science and Technology
To link to this article: https://doi.org/10.1080/02670836.2018.1440155

Figure 8. ILS in A_A (a) and A_BC (b) structure vs. drawing strain. The calculated ILS is based on a $\varepsilon^{-0.5}$ power-law relationship [Reprinted from ref 15, with permission from Elsevier].

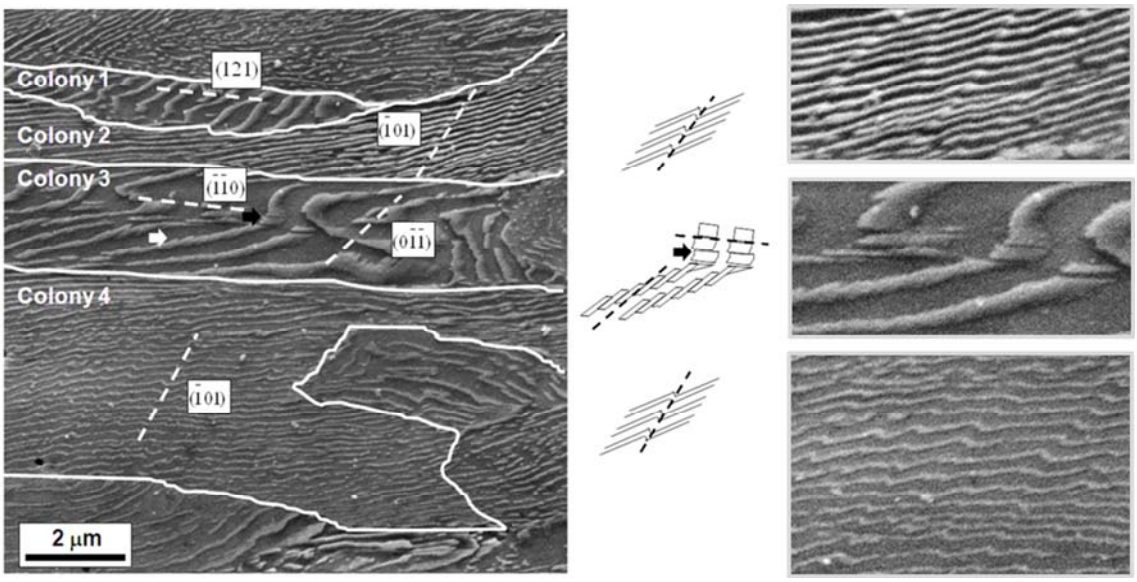

Figure 9. SEM micrographs showing the cementite morphology at the strain of 0.68 in the longitudinal section. Traces of the {110} and {112} slip planes of ferrite are shown, as determined from EBSD orientation measurement. Thick white lines are ferrite colony boundaries. Enlarged areas and schematics of coarse slip steps, shear bands and cracks are shown on the right side. [Reprinted from ref 21, with permission from Elsevier]

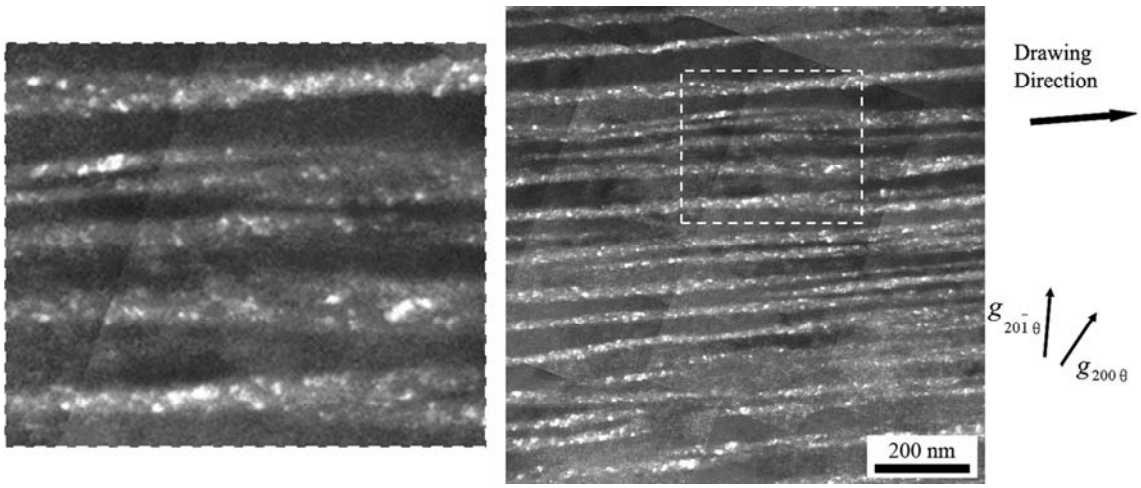

Figure 10. Dark field images (using cementite diffraction spots) in the longitudinal section of the wire at the strain of 1.51. The dashed line framed area has been enlarged and shown on the left. The cementite nanocrystals have their sizes is in the range up to the cementite lamellae thickness.

Please cite this paper as following: Xiaodan Zhang, Niels Hansen, Andrew Godfrey & Xiaoxu Huang (2018): Structure and strength of sub-100 nm lamellar structures in cold-drawn pearlitic steel wire, Materials Science and Technology
To link to this article: https://doi.org/10.1080/02670836.2018.1440155

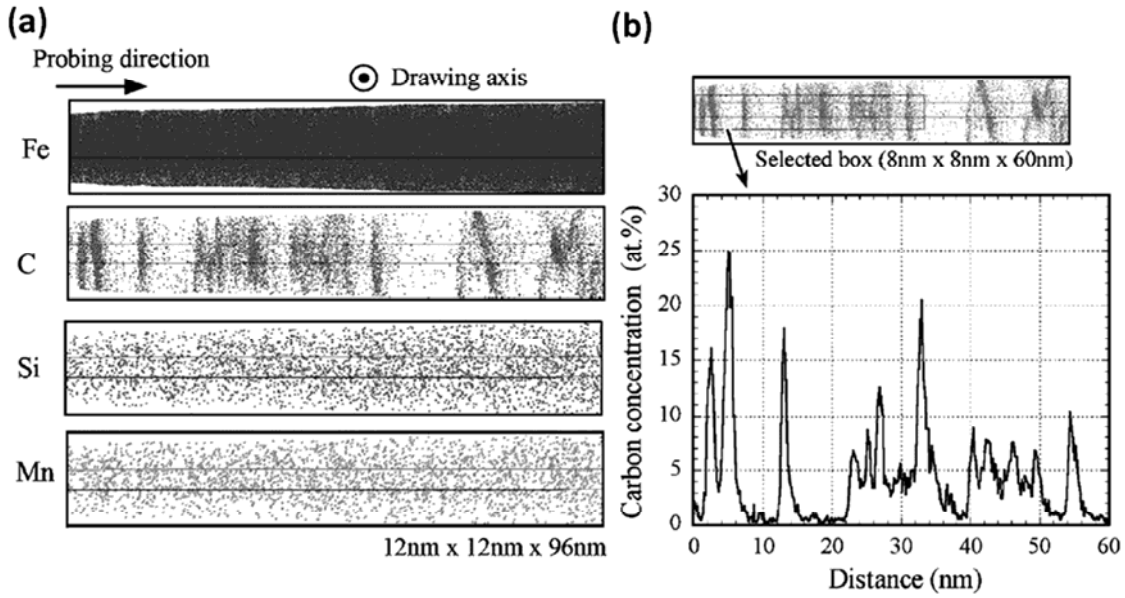

Figure 11. (a) 3D elemental maps and (b) carbon concentration profile perpendicularly intersecting the lamellar structure by 3DAPT in a pearlitic steel wire with 0.8 wt.% C at a strain of 5 [Reprinted from ref 61, with permission from Elsevier].

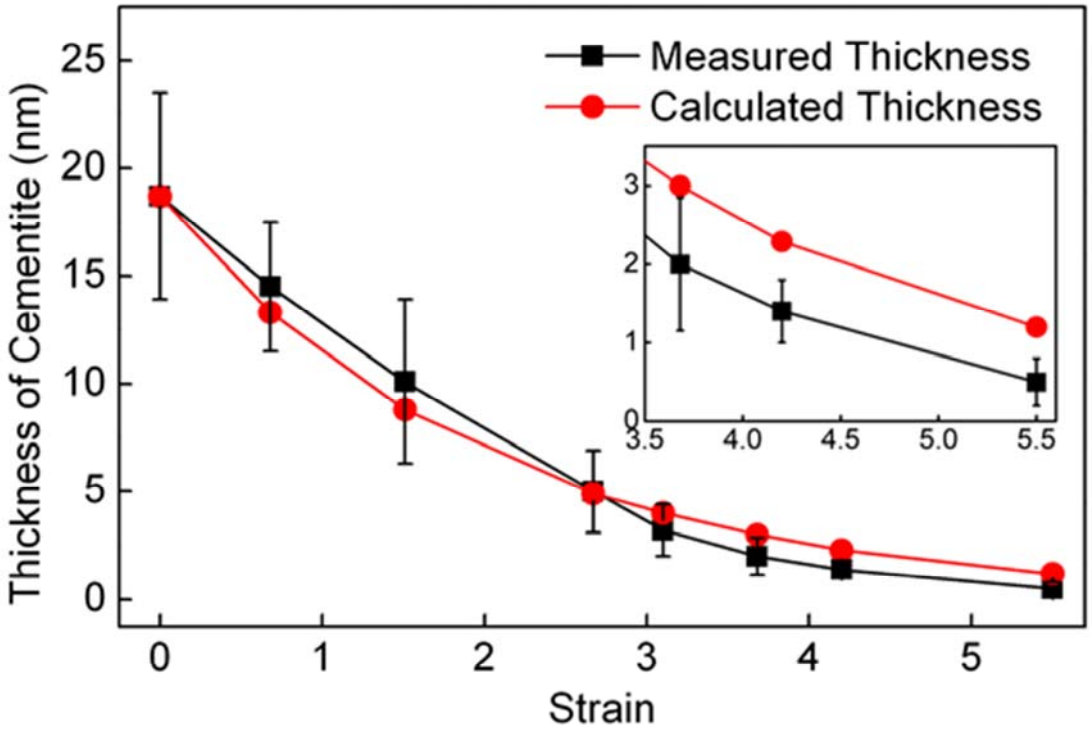

Figure 12. Thickness of cementite versus drawing strain. The calculated reduction in thickness of cementite is obtained on the assumption that they deform in accordance with the reduction in wire diameter (Eq. (1)). The thickness of cementite at high strains

Please cite this paper as following: Xiaodan Zhang, Niels Hansen, Andrew Godfrey & Xiaoxu Huang (2018): Structure and strength of sub-100 nm lamellar structures in cold-drawn pearlitic steel wire, Materials Science and Technology
To link to this article: https://doi.org/10.1080/02670836.2018.1440155

is magnified and shown in the box. It is shown that the transition zone appears at the strain range from 2.7 to 3.7. [Reprinted from ref 11, with permission from Elsevier]

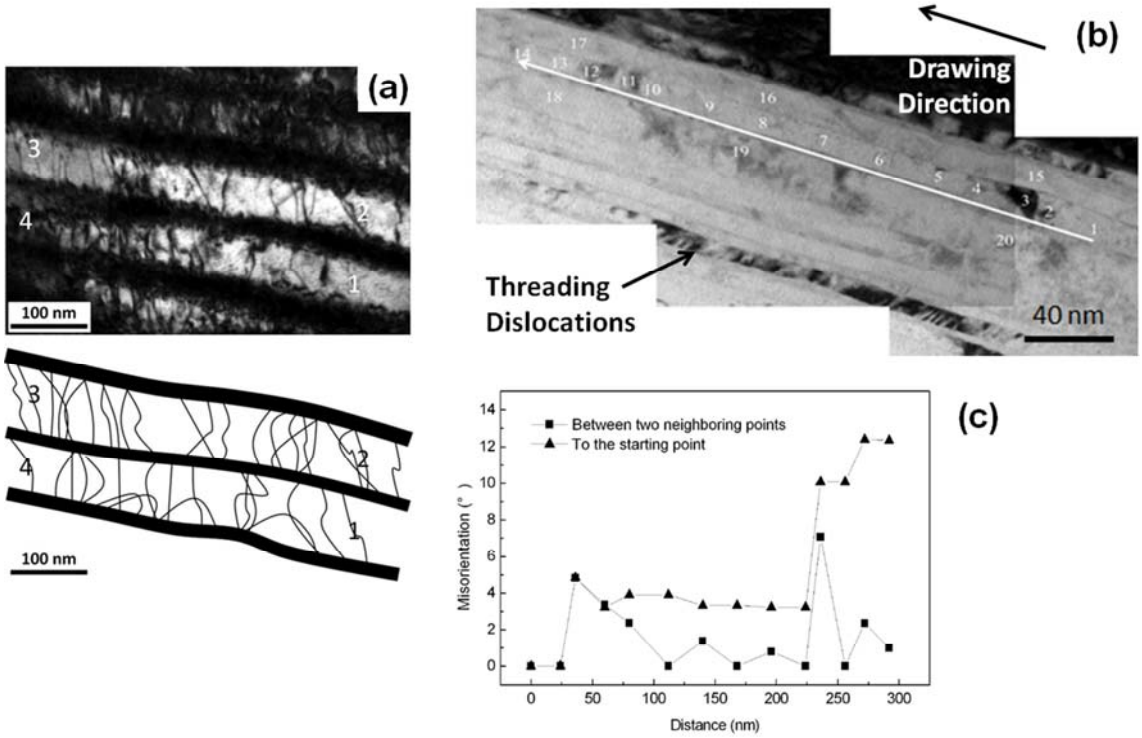

Figure 13. Dislocation structures in the ferrite lamellae: (a) TEM micrograph of a sample deformed to a strain of 1.5 and a sketch of the dislocation structure where the thick lines represent cementite lamellae and the thin lines represent dislocations, (b) TEM micrograph of a sample deformed to a strain of 3.7 with numbers 1-20 representing the crystallographic orientation measuring points and (c) Crystallographic orientation change along the white arrow in (b) plotted versus their distances from the starting points. The dislocations are stored as threading dislocations and dislocation tangles. [Reprinted from ref 9 and 15, with permission from Elsevier]

Please cite this paper as following: Xiaodan Zhang, Niels Hansen, Andrew Godfrey & Xiaoxu Huang (2018): Structure and strength of sub-100 nm lamellar structures in cold-drawn pearlitic steel wire, Materials Science and Technology
To link to this article: https://doi.org/10.1080/02670836.2018.1440155

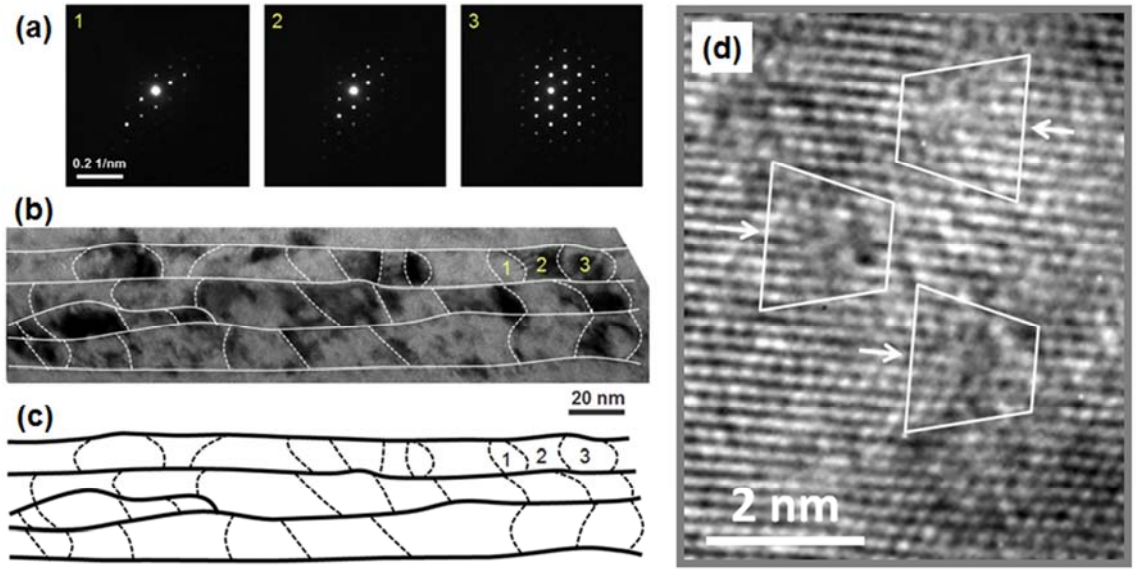

Figure 14. Nanobeam diffraction, TEM, and HREM micrographs showing the low angle dislocation boundaries in the cold-drawn pearlitic steel wire at the strain of 5.4. The visibility of the dislocation content in low angle dislocation boundaries in the ferrite lamellae provides a powerful tool to measure the dislocation density at high strain [Reprinted from ref 11, with permission from Elsevier].

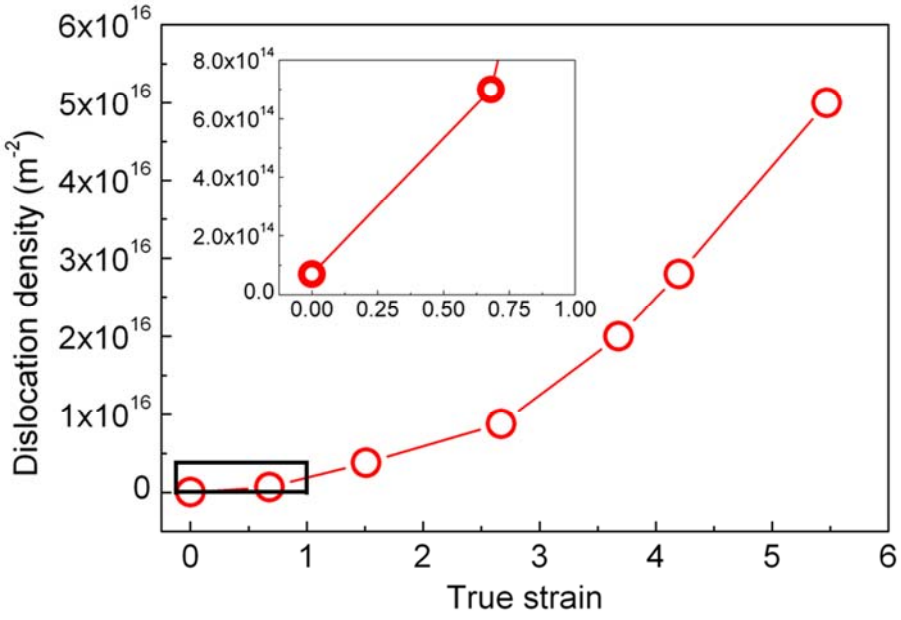

Figure 15. Dislocation density in the ferrite lamellae versus the drawing strain. For drawing strains less than 1 the magnified data are shown in the box. The dislocation density increases with an increasing rate through a transition region (see text) [Reprinted from ref 11, with permission from Elsevier].

Please cite this paper as following: Xiaodan Zhang, Niels Hansen, Andrew Godfrey & Xiaoxu Huang (2018): Structure and strength of sub-100 nm lamellar structures in cold-drawn pearlitic steel wire, Materials Science and Technology
To link to this article: https://doi.org/10.1080/02670836.2018.1440155

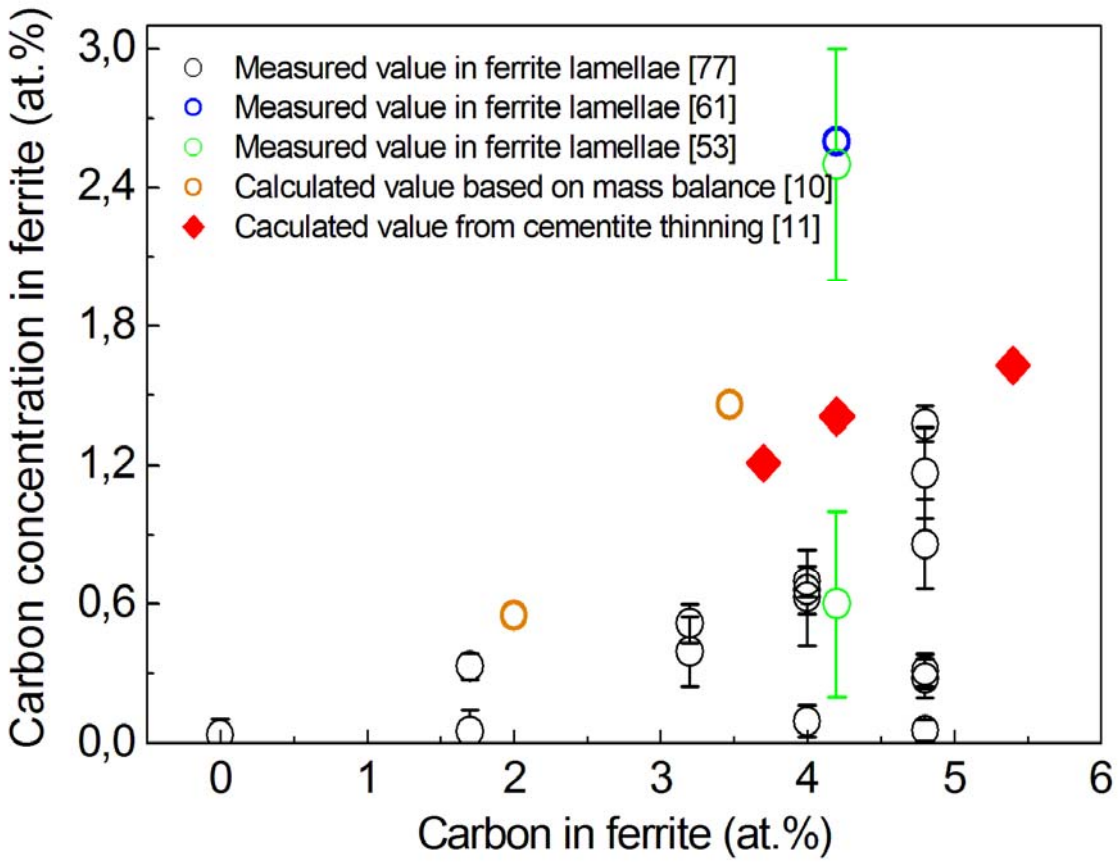

Figure 16. Carbon content in the ferrite lamellae versus the true strain measured by 1DAPFIM and 3DAPM and calculated as a mass balance based on measured carbon concentration in cementite by 3DAPM and based on thinning of cementite lamellae. [Reprinted from ref 11, with permission from Elsevier].

Please cite this paper as following: Xiaodan Zhang, Niels Hansen, Andrew Godfrey & Xiaoxu Huang (2018): Structure and strength of sub-100 nm lamellar structures in cold-drawn pearlitic steel wire, Materials Science and Technology
To link to this article: https://doi.org/10.1080/02670836.2018.1440155